



An anionic surfactant-assisted equilibrium adsorption method to prepare highly dispersed Fe-promoted Ni/Al₂O₃ catalysts for highly selective mercaptan removal



Tingting Huang, Qingyi Peng, Wenjin Shi, Jundong Xu, Yu Fan*

State Key Laboratory of Heavy Oil Processing, China University of Petroleum, Beijing 102249, PR China

ARTICLE INFO

Keywords:
 Ni/Al₂O₃
 Fe promoter
 High dispersion
 Thioetherification catalyst
 Mercaptan removal

ABSTRACT

This article proposes a novel sodium dodecylbenzenesulfonate (SDBS)-assisted equilibrium adsorption method for preparing highly dispersed Ni/Al₂O₃ and Fe-promoted NiFe/Al₂O₃ thioetherification catalysts. The proposed strategy anchors nickel cations onto the electronegative surface of an Al₂O₃ support modified by negatively charged DBS⁻ bilayers. As a result, this method achieves highly dispersed Ni nanoparticles without strengthening the metal-support interaction, promoting the reducibility and sulfurization of the supported Ni species. The as-prepared Ni-based catalysts have a smaller size, a higher dispersion of metal nanoparticles, and a greater amount of active metal sulfides than their counterparts prepared by the conventional impregnation method, endowing them with excellent catalytic performance for the highly selective removal of mercaptans. This method provides a new opportunity to prepare highly dispersed metal nanoparticles without a strong metal-support interaction.

1. Introduction

With increasingly stringent environmental regulations, the restrictions on the sulfur content of gasoline are becoming more and more stringent [1–4]. Mercaptans are the most detrimental sulfur-containing compounds in gasoline, not only because they are foul smelling and corrosive [5,6] but also because they can degrade gasoline quality by promoting the formation of gum [7]. Therefore, to produce clean gasoline, it is imperative to remove mercaptans from gasoline. The Merox sweetening process is the most typical technique for mercaptan removal. Although the improved fixed-bed sweetening technology has reduced the usage of sodium hydroxide, there is still a problem with the discharge of caustic dross [8,9]. Furthermore, mercaptans can also be removed by the hydrodesulfurization (HDS) technique, but this process saturates a large number of olefins that contribute to the octane number of gasoline; therefore, the HDS technique degrades the quality of the resultant gasoline product [10,11]. The thioetherification technique is usually carried out at low temperature under a H₂ atmosphere, in which the mercaptans in gasoline react with diolefins to form thioethers that can be removed in the subsequent process along with any sulfur-containing compounds with higher boiling points [12,13]. During the thioetherification process, the mercaptans in gasoline are removed while avoiding olefin saturation and maintaining the gasoline octane number.

Solid acids and sulfided transition metals have been applied to the thioetherification process [14,15]. Solid acid catalysts, such as sulfonic acid resin, solid phosphoric acid and intercalation compound, are effective catalysts for the thioetherification of mercaptans, but they are strong acid catalysts [14], which interact strongly with the basic nitrogen-containing compounds. Therefore, nitrogen-containing compounds are difficult to desorb from these strong acid sites, resulting in the deactivation of solid acid catalysts [14,16]. Sulfided transition metals (Ni, Pt, Pd and Ag) also have catalytic activity for the thioetherification of mercaptans [15,17,18]. In particular, low-cost nickel-based catalysts exhibit excellent sulfur and nitrogen resistance and good thioetherification activity [19], and thus, they have been applied in the thioetherification process [13]. In recent years, the Fe-promoted Ni/Al₂O₃ catalysts were also investigated and they exhibited better catalytic activity than the monometallic Ni/Al₂O₃ in the thioetherification for removing methyl and ethyl mercaptans [20]. For supported Ni/Al₂O₃ catalysts, their activity and selectivity depend on the type and quantity of active sites, which are greatly affected by the dispersion and reduction degree of metal particles. Akande et al. reported that the reduction degree of nickel species is strongly affected by the nanoparticle size of nickel oxides: smaller nanoparticles can lead to a higher reduction degree and confer the synthesized catalysts with improved catalytic performance [21].

* Corresponding author.

E-mail address: fanyu@cup.edu.cn (Y. Fan).

In general, the incipient wetness impregnation method, nickel-alumina co-precipitation method and sol-gel method are the main approaches for synthesizing nickel-based catalysts [22–24]. The catalysts prepared by traditional impregnation method have large metal Ni particles, resulting in inferior utilization of nickel species [25]. Although the co-precipitation and sol-gel methods are desirable for increasing the dispersion of nickel species, the strong metal-support interaction results in a substantial increase in the difficulty in nickel reduction and sulfidation [26]. Li et al. investigated nickel species, nickel particle size, and nickel reducibility over three nickel catalysts prepared by the co-precipitation, sol-gel, and impregnation methods. Their results showed that the co-precipitation and sol-gel methods strengthened the interaction between the nickel species and alumina support and generated a large amount of NiAl_2O_4 spinel phase, which is detrimental to the subsequent formation of the active phase [26].

In addition, Zhu et al. reported that the plasma treatment method is conducive to decreasing the nickel particle size and improving nickel dispersion, but it still suffers from the problem of the enhancement of the metal-support interaction [27]. Seo et al. proposed a single-step sol-gel and subsequent CO_2 supercritical drying method that is suitable for producing well-dispersed $\text{Ni}/\text{Al}_2\text{O}_3$ catalysts with uniformly distributed nickel nanoparticles, but this method is performed under high pressure and requires a high-cost device [28]. In summary, the preparation of $\text{Ni}/\text{Al}_2\text{O}_3$ catalysts with high metal dispersion and a weak metal-alumina interaction remains a great challenge.

Herein, we proposed a sodium dodecylbenzenesulfonate (SDBS)-assisted equilibrium adsorption (SDEA) method to prepare highly dispersed $\text{Ni}/\text{Al}_2\text{O}_3$ and $\text{NiFe}/\text{Al}_2\text{O}_3$ catalysts without strengthening the metal-support interaction. In this method, the negatively charged DBS⁻ ions could form self-assembled bilayers on the Al_2O_3 surface; one negative charge in these bilayers is connected with the electropositive Al_2O_3 surface, and the other negative charge is exposed, which converts the positively charged Al_2O_3 support into a negatively charged Al_2O_3 support modified by DBS⁻ ($\text{Al}_2\text{O}_3\text{-DBS}$). Therefore, Ni^{2+} ions can be anchored to the electronegative surface of $\text{Al}_2\text{O}_3\text{-DBS}$ via electrostatic adsorption. Meanwhile, this method weakens the metal-support interaction and reduces the formation of nickel-alumina spinels because it decreases the direct interaction between Ni species and the alumina support. As a consequence, the high dispersion of the supported nickel species does not depend on the metal-support interaction. The as-prepared Ni-based catalysts featured highly dispersed Ni nanoparticles with enhanced reducibility and sulfurization degree and thus exhibited excellent performance in the selective removal of mercaptans.

2. Experimental

2.1. Materials

The shaped Al_2O_3 support was obtained from Shandong Alumina Plant (PR China). Nickel nitrate ($(\text{Ni}(\text{NO}_3)_2\cdot 6\text{H}_2\text{O}$, 99%), ferric nitrate ($(\text{Fe}(\text{NO}_3)_3\cdot 9\text{H}_2\text{O}$, 98%), sodium dodecylbenzenesulfonate (SDBS, 98%) and hydrochloric acid (HCl, 37%) were purchased from J&K Chemical Technology Company, Ltd. (PR China). 1-Propanethiol, 1-butanethiol, iso-butanethiol, t-butanethiol, 1-pantanethiol, 1-octene, isoprene, octane, toluene, carbon disulfide (CS_2) and cyclohexane were purchased from Aladdin Biochemical Company (PR China) and used directly without any further purification.

2.2. Catalyst preparation

The preparation of the Ni-SDEA catalyst involves the following steps: 1.0 g of Al_2O_3 was added into 70 mL of deionized water, and the resulting suspension was adjusted to $\text{pH} = 5.0$ by HCl. Then, 4.68 g of SDBS was slowly added, the suspension was magnetically stirred until SDBS dissolved completely, and the mixture was acidified to $\text{pH} = 5.0$ by HCl. Subsequently, 1.30 g of $\text{Ni}(\text{NO}_3)_2\cdot 6\text{H}_2\text{O}$ was added into the

mixture and then stirred for 4 h at 25 °C. The resulting mixture was placed in a 100 mL autoclave and heated at 120 °C for 24 h under rotation. Next, the sample was filtered, washed with deionized water until pH 7 was reached, and dried at 120 °C overnight. Subsequently, the sample was calcined in muffle furnace at a ramp rate of 2 °C/min from room temperature to 500 °C and maintained at this temperature for 4 h. The calcinations were carried out in muffle furnace without the introduction of flowing air. The obtained product is denoted Ni-SDEA.

For comparison, the Ni-IM catalyst was prepared by incipient wetness impregnation as follows: Al_2O_3 was impregnated with a $\text{Ni}(\text{NO}_3)_2$ aqueous solution. Then, the sample was prepared using the same drying and calcination steps as those described for Ni-SDEA. According to the inductively coupled plasma (ICP) results, the NiO loadings of Ni-SDEA and Ni-IM were 13.8 and 14.0 wt.%, respectively.

The loading of Fe in the Ni-SDEA and Ni-IM catalysts was carried out by impregnating Ni-SDEA and Ni-IM with $\text{Fe}(\text{NO}_3)_3$. The impregnated samples were dried at 120 °C overnight and calcined at 500 °C in air for 4 h. The obtained products were denoted NiFe-SDEA and NiFe-IM. The Fe_2O_3 contents in NiFe-SDEA and NiFe-IM were 6.0 and 5.9 wt.% (determined by ICP analysis), respectively.

The Fe-IM catalyst was prepared by impregnating Al_2O_3 with a $\text{Fe}(\text{NO}_3)_3$ aqueous solution. The sample was prepared using the same steps as those described for Ni-IM. The Fe_2O_3 loading of Fe-IM was 6.1 wt.% (determined by ICP analysis).

The sulfided catalysts were obtained by sulfurizing the oxidic catalysts with 3 wt.% CS_2 in cyclohexane at 230, 280, 300 and 320 °C respectively for 2 h in a fixed-bed microreactor. The sulfurization processes were performed at 2.0 MPa, a liquid hourly space velocity (LHSV) of 4 h^{-1} , and a H_2/oil ratio of 300 (v/v). The oxidic catalysts are denoted as Ni-SDEA, Ni-IM, NiFe-SDEA, NiFe-IM and Fe-IM; the corresponding sulfided catalysts are denoted as NiS-SDEA, NiS-IM, NiFeS-SDEA, NiFeS-IM and FeS-IM.

2.3. Characterization

X-ray diffraction (XRD) was carried out on a Bruker D8 Advance X-ray diffractometer with $\text{Cu K}\alpha$ radiation at 40 kV and 40 mA. The scanning rate was 5°/min over the angular range from 10 to 90°. N_2 adsorption-desorption experiments were performed using a Micromeritics ASAP 2420 instrument. Prior to the adsorption measurement, the samples were evacuated at 250 °C overnight. The compositions of samples were determined by ICP on a PerkinElmer OPTIMA 7000 DV spectrometer. Before the measurements, the samples were dissolved in *aqua regia*. The zeta potentials of the samples were determined by a Zetasizer Nano ZS instrument. The ammonia temperature-programmed desorption ($\text{NH}_3\text{-TPD}$) experiments were carried out on a Builder PCA-1200 instrument. First, 0.1 g of the sample was heated from 30 to 600 °C under Ar (30 mL (STP)/min), and the temperature was kept at 600 °C for 0.5 h. Then, the quartz reactor was cooled to 70 °C in Ar, and NH_3 (30 mL (STP)/min) was passed into the reactor at that temperature for 20 min; subsequently, the sample was purged with Ar at 70 °C for 90 min to remove the physically adsorbed NH_3 . Finally, the sample was heated to 600 °C in an Ar flow at a heating rate of 10 °C min^{-1} , and the signal of the desorbed ammonia was recorded with a thermal conductivity detector (TCD). The hydrogen temperature-programmed reduction ($\text{H}_2\text{-TPR}$) experiments were performed on an AutoChem II 2920 (Micromeritics, USA). Typically, 0.1 g of the sample was pretreated in a quartz reactor at 450 °C for 2 h in an Ar flow (30 mL (STP)/min) and then cooled down to 60 °C. Subsequently, the sample was heated to 1000 °C in a 10 vol % H_2/Ar mixture (30 mL (STP)/min) at a heating rate of 10 °C min^{-1} , and a calibration curve of the TCD response signal expressed by the integrated area of the peak as a function of the amount of consumed hydrogen was established with a series of known amounts of pure CuO samples [29]. The CO chemisorption of the samples was carried out on AutoChem II 2920 (Micromeritics, USA). Typically, 0.2 g of the sulfided sample was heated at

300 °C for 2 h in a He flow (at 30 mL/min) and subsequently was cooled down to –50 °C. Then, pulse chemisorption measurements were conducted at –50 °C with 10% CO in He atmosphere. The H₂ chemisorption of the sulfided samples was carried out on AutoChem II 2920 (Micromeritics, USA). 0.2 g sample was introduced into a quartz reactor, and after reduction in H₂ at 500 °C for 2 h, the sample was kept at 500 °C for 30 min in a He flow. Then, the sample was cooled down to 25 °C with 10% H₂ in He atmosphere. To calculate metal dispersion, the adsorption stoichiometry of H/Ni = 1 was assumed [30]. X-ray photoelectron spectroscopy (XPS) analysis of the samples was carried out on a VG ESCA Lab 250 spectrometer using Al K α radiation with an energy resolution of 0.4 eV. The spectra were scanned at a pressure of 3×10^{-8} Pa. High-resolution transmission electron microscopy (HRTEM) was performed on an F20 microscope at an acceleration voltage of 200 kV. The size distribution of metal nanoparticles was determined by manual measurement of the particles in 20 HRTEM images from each sample. Energy dispersive spectroscopy (EDS) was performed on the energy dispersive X-ray instrument attached to the TEM system. The carbon content of the calcined catalyst was determined on a Leco CS600 carbon analyzer [31].

2.4. Assessment of catalyst activity

The thioetherification activities were evaluated in a fixed-bed microreactor with a loading of 1.0 g of catalyst (20–40 mesh) using a mixture of mercaptan (0.048 wt%), 1-octene (23.0 wt%), isoprene (0.4 wt%), octane (46.6 wt%) and toluene (30.0 wt%) as a model system. The reactions were carried out at 1.0 MPa, 135 °C (determined from Fig S1), a liquid hourly space velocity (LHSV) of 6 h⁻¹ (determined from Fig S2), and a H₂/oil ratio of 30 (v/v) over the sulfided catalyst. The products were collected after a steady state was reached. The sulfur compounds in the products were analysed using a TSQ 8000 Evo GC-MS with an HP-5ms chromatographic column (60 m × 0.25 mm × 0.25 μm). The hydrocarbon compositions in the products were analysed using an Agilent 1790 gas chromatograph (GC) equipped with a flame ionization detector (FID) and an HP-PONA capillary column (50 m × 0.20 mm × 0.50 μm).

Mercaptan removal ratio (r_{mer}) and olefin conversion (X_{ole}) were defined as follows:

$$r_{mer} = \frac{\text{mass fraction of mercaptan in feed} - \text{mass fraction of mercaptan in product}}{\text{mass fraction of mercaptan in feed}} \times 100\% \quad (1)$$

$$X_{ole} = \frac{\text{mass fraction of olefin in feed} - \text{mass fraction of olefin in product}}{\text{mass fraction of olefin in feed}} \times 100\% \quad (2)$$

The turnover frequency (TOF) was used to evaluate the thioetherification activity. The TOF was calculated by the following equation:

$$TOF = \frac{F_{Ao}}{W} \frac{X_A}{CO_{uptake}} \quad (3)$$

where F_{Ao} is the molar rate of 1-propanethiol fed into the reactor (μmol s⁻¹), W is the catalyst weight (g), CO_{uptake} is the uptake of chemisorbed CO (μmol g⁻¹), and X_A is the 1-propanethiol conversion (%).

3. Results and discussion

3.1. Characterization of the oxidic Ni/γ-Al₂O₃, NiFe/γ-Al₂O₃ and Fe/γ-Al₂O₃ catalysts

3.1.1. XRD

The XRD patterns of the Ni-SDEA and Ni-IM catalysts and the γ-Al₂O₃ support are shown in Fig. 1(a). The diffraction peaks at 2θ = 36.9°, 39.4°, 46.0° and 66.8° are ascribed to γ-Al₂O₃ (JCPDS No.

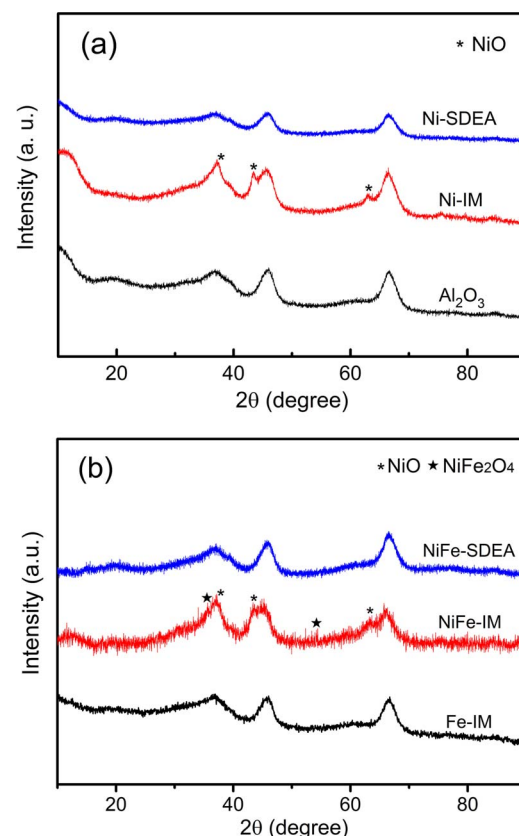


Fig. 1. XRD patterns of the oxidic Ni/Al₂O₃ catalysts and Al₂O₃ (a) and the oxidic NiFe/Al₂O₃ and Fe/Al₂O₃ catalysts (b).

29-1486) [32,33]. Only the Ni-IM catalyst possesses the NiO diffraction peaks at 2θ = 37.3°, 43.4° and 62.8° (JCPDS No. 44-1159) [34], indicating that it has a large particle size and a low dispersion of NiO. However, the Ni-SDEA catalyst has no bulk NiO crystallite peak in its XRD pattern, suggesting that it has a small particle size and a high dispersion of NiO. Compared with the Ni-IM catalyst prepared by the impregnation method, the Ni-SDEA catalyst prepared by the SDEA method has smaller NiO particles and better NiO dispersion.

The XRD patterns of the NiFe-SDEA, NiFe-IM and Fe-IM catalysts are shown in Fig. 1(b). There are no Fe₂O₃ diffraction peaks in the XRD pattern of Fe-IM because of the low Fe loading. In addition, no peaks assigned to NiO and NiFe₂O₄ crystallites are observed in the XRD pattern of NiFe-SDEA, demonstrating that the metal oxides are highly dispersed on the support. In the pattern of NiFe-IM, the peaks at 2θ = 37.3°, 43.4° and 62.8° are ascribed to the aggregation of NiO species (JCPDS No. 44-1159) [35], and the peaks at 2θ = 35.7° and 54.0° are attributed to the bulk NiFe₂O₄ species (JCPDS No. 54-0964) [36]. The above results reveal that the crystallites of metal oxides over NiFe-SDEA are smaller than those over NiFe-IM.

3.1.2. XPS

The catalytic activity and selectivity of the thioetherification catalysts are affected by the number and chemical states of surface active metal sites. XPS characterization results can be used to determine the surface nickel components and dispersion degree. The high-resolution scans and corresponding fitting curves of Ni 2p spectra over the Ni-SDEA and Ni-IM catalysts are shown in Fig. 2. According to the peak area of the fitting curves, the calculated Ni/Al atomic ratios on the Ni-SDEA and Ni-IM catalysts are 0.085 and 0.074, respectively (Table 1). The above two catalysts were prepared with the same γ-Al₂O₃ support and almost equal NiO contents (about 14.0 wt%, as determined by ICP); therefore, the Ni/Al atomic ratio can be used as a measurement to

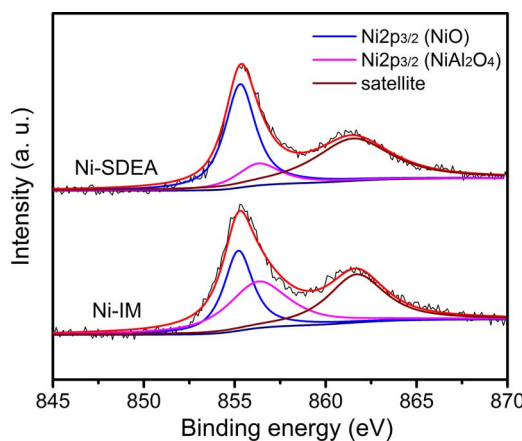
Fig. 2. Ni 2p XPS spectra of the oxidic Ni/Al₂O₃ catalysts.

Table 1
Fitting results of XPS and NH₃-TPD results on Ni-SDEA and Ni-IM catalysts.

Catalyst	Ni/Al	Ni 2p _{3/2} (%)		Acid amount (relative content)
		NiO	NiAl ₂ O ₄	
Ni-SDEA	0.085	76.7	23.3	1.00
Ni-IM	0.074	45.0	55.0	0.99

compare the dispersion degrees of Ni-SDEA and Ni-IM. The results show that Ni-SDEA has a higher Ni/Al atomic ratio than Ni-IM, indicating that the NiO particles on Ni-SDEA are highly dispersed.

The binding energy at 855.5 eV is assigned to the spin-orbit split lines of Ni 2p_{3/2}, and the binding energy at 861.5 eV is ascribed to the shake-up satellites of Ni 2p_{3/2} [37]. For the Ni 2p_{3/2} energy level, two peaks are observed at 855.2 and 856.3 eV, which are attributed to octahedral Ni²⁺ of the NiO species and tetrahedral Ni²⁺ of the NiAl₂O₄ phase, respectively [38]. According to the high-resolution scans and corresponding fitting curves of the Ni 2p_{3/2} spectra, the relative concentrations of different Ni²⁺ species were derived, as presented in Table 1. The relative contents of NiO and NiAl₂O₄ species in Ni-SDEA are 76.7% and 23.3%, respectively, and the relative contents of NiO and NiAl₂O₄ species in Ni-IM are 45.0% and 55.0%, respectively. Clearly, compared to Ni-IM, Ni-SDEA has a higher NiO content and a lower NiAl₂O₄ content, indicating that the implementation of the SDEA method weakens the interaction between the γ-Al₂O₃ support and nickel species, thereby hindering the formation of inactive NiAl₂O₄ species and increasing the relative content of NiO species.

The different Ni species on NiFe-SDEA and NiFe-IM are studied using the XPS survey spectra shown in Fig. 3(a). Compared with monometallic Ni-SDEA and Ni-IM, the new XPS peak at 855.6 eV is assigned to Ni in NiFe₂O₄ species [39], and the binding energies of the Ni 2p_{3/2} level shift to lower values, indicating the enhanced electron density of the nickel oxide species due to the addition of Fe₂O₃ to Ni/Al₂O₃ [40]. According to the high-resolution scans and corresponding fitting curves of the Ni 2p_{3/2} spectra, the contents of different Ni species were derived, as presented in Table 2. The content of Ni in NiFe₂O₄ species is 33.6% for NiFe-SDEA and 22.7% for NiFe-IM; the total content of Ni in NiO and NiFe₂O₄ species, which are precursors of the active sites Ni_x and NiFeS_x, increases from 50.5% in NiFe-IM to 76.7% in NiFe-SDEA. In addition, the content of Ni in NiAl₂O₄ species in NiFe-SDEA is much lower than that in NiFe-IM.

The Fe 2p_{3/2} XPS spectra of the NiFe-SDEA, NiFe-IM and Fe-IM catalysts are exhibited in Fig. 3(b). On the surface of NiFe-SDEA, NiFe-IM and Fe-IM, the Fe species exist as NiFe₂O₄, FeO, Fe₂O₃ and Fe-O-Al [41]. In the bimetallic NiFe catalysts, the binding energies of different Fe species exhibit slight changes compared with those in monometallic

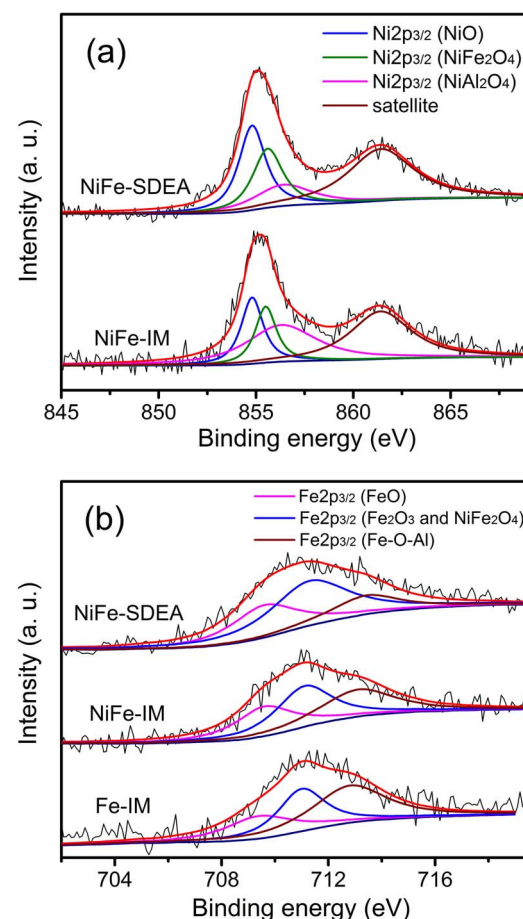


Fig. 3. Ni 2p XPS spectra of NiFe-SDEA and NiFe-IM (a) and Fe 2p XPS spectra of NiFe-SDEA, NiFe-IM and Fe-IM (b).

Table 2
XPS fitting results of NiFe-SDEA, NiFe-IM and Fe-IM.

Catalyst	Ni 2p _{3/2} (%)			Fe 2p _{3/2} (%)		
	Ni ²⁺ in NiO	Ni ²⁺ in NiFe ₂ O ₄	Ni ²⁺ in NiAl ₂ O ₄	Fe ²⁺ in FeO	Fe ³⁺ in Fe ₂ O ₃ and NiFe ₂ O ₄	Fe ³⁺ in Fe-O-Al
NiFe-SDEA	43.1	33.6	23.4	30.8	50.9	18.4
NiFe-IM	27.8	22.7	49.5	28.8	37.9	33.3
Fe-IM	—	—	—	24.4	32.0	43.7

Fe/Al₂O₃, indicating that the chemical environment and electronic state of Fe are influenced by Ni [42]. The Fe 2p_{3/2} spectra are decomposed according to the literature [43], and the relative contents of Fe in NiFe₂O₄, FeO, Fe₂O₃ and Fe-O-Al species are listed in Table 2. Compared with Fe-IM, the contents of Fe in Fe-O-Al species of NiFe-SDEA and NiFe-IM decrease because the formation of NiFe₂O₄ species involves Fe³⁺ and Ni²⁺ species, which can inhibit the generation of Fe-O-Al species. In addition, the content of Fe in Fe-O-Al decreases from 33.3% of NiFe-IM to 18.4% of NiFe-SDEA. These results demonstrate that the incorporation of SDBS into the preparation process weakens the metal-support interaction, thereby reducing the generation of inactive Fe-O-Al species and promoting the formation of more NiFe₂O₄ species.

3.1.3. N₂ adsorption-desorption

The nitrogen adsorption-desorption isotherms and the pore diameter distributions of Ni/γ-Al₂O₃, NiFe/γ-Al₂O₃, Fe/γ-Al₂O₃ and γ-Al₂O₃ indicate that the five catalysts and the support have mesoporous structures with concentrated pore size distributions (Figs. S3 and S4).

Table 3

Textural properties results of Ni-SDEA, Ni-IM, NiFe-SDEA, NiFe-IM and Fe-IM catalysts and Al_2O_3 support.

Sample	S_g^a ($\text{m}^2 \text{g}^{-1}$)	V_p^b ($\text{cm}^3 \text{g}^{-1}$)	D_p^c (nm)
Ni-SDEA	272	0.47	7.1
Ni-IM	238	0.34	6.2
NiFe-SDEA	259	0.41	6.8
NiFe-IM	221	0.29	6.0
Fe-IM	291	0.51	7.1
Al_2O_3	315	0.63	7.2

^a BET specific surface area.

^b Pore volume.

^c Most probable pore size obtained by N_2 adsorption–desorption.

The most probable pore size of Ni-SDEA is higher than that of Ni-IM and close to that of $\gamma\text{-Al}_2\text{O}_3$ (Figs. S3 and S4), and the most probable pore size of NiFe-SDEA is higher than that of NiFe-IM, implying that the SDEA method has a negligible influence on the pore size of the $\gamma\text{-Al}_2\text{O}_3$ support.

The textural properties of the samples are listed in Table 3. Compared with the support, the pore volume and surface area of Ni/ $\gamma\text{-Al}_2\text{O}_3$, NiFe/ $\gamma\text{-Al}_2\text{O}_3$, and Fe/ $\gamma\text{-Al}_2\text{O}_3$ decrease. This is because during the calcination process, the supported active metal precursors yield deposited nanoparticles, which plug and block the pore channels of the support. Compared with the Ni-SDEA and NiFe-SDEA catalysts prepared by the SDEA method, the pore volume and surface area of Ni-IM and NiFe-IM catalysts prepared by the incipient wetness impregnation method decrease dramatically, this is because the supported metal nanoparticles are highly dispersed on Ni-SDEA and NiFe-SDEA, and the pore channels of the support are retained well. The introduction of Fe_2O_3 into the Ni-SDEA and Ni-IM catalysts results in the decreased surface areas and pore volumes in them, due to the blockage of pores in the support by the incorporated Fe_2O_3 . Compared with other catalysts, Fe-IM has a larger surface area and pore volume, which are attributed to the lower metal loading.

3.1.4. H_2 -TPR

To analyse the reducibility of metal oxides over the $\text{NiO}/\text{Al}_2\text{O}_3$ catalysts, the Ni-SDEA and Ni-IM catalysts were evaluated using H_2 -TPR experiments, and the results are displayed in Fig. 4(a). All the samples have two H_2 consumption peaks in the range of 400–820 °C. The peaks at low temperature over these two catalysts correspond to the reduction of NiO species strongly interacting with $\gamma\text{-Al}_2\text{O}_3$ [20], and the peaks at high temperature over these two catalysts are attributed to the reduction of NiAl_2O_4 spinels [39,44,45]. The H_2 consumption peaks at low and high temperatures of Ni-SDEA are 539 and 726 °C, respectively, while those of Ni-IM are 590 and 750 °C, demonstrating that the metal-support interaction is weaker over Ni-SDEA than over Ni-IM. The total hydrogen consumptions in the H_2 -TPR patterns of Ni-SDEA and Ni-IM are quantified to be 1.426 and 1.125 mmol g⁻¹, respectively. The corresponding H_2 consumption of the peak at low temperature was obtained by peak decomposing. The H_2 consumptions over Ni-SDEA and Ni-IM at low temperature are 1.184 and 0.909 mmol g⁻¹, respectively, which is consistent with the higher NiO quantity and smaller particles in Ni-SDEA than in Ni-IM.

The H_2 -TPR profiles of NiFe-SDEA, NiFe-IM and Fe-IM are presented in Fig. 4(b). The profile of Fe-IM shows two reduction peaks at 388 and 528 °C, which are ascribed to the reduction of $\alpha\text{-Fe}_2\text{O}_3$ to Fe_3O_4 and the reduction of Fe_3O_4 to $\alpha\text{-Fe}$, respectively [46,47]. For the NiFe-SDEA catalysts, the peak at 311 °C is attributed to the reduction of $\alpha\text{-Fe}_2\text{O}_3$ to Fe_3O_4 , and the peak at 512 °C corresponds to the reduction of Fe_3O_4 to $\alpha\text{-Fe}$, the reduction of NiO species weakly interacting with $\gamma\text{-Al}_2\text{O}_3$ to Ni, and the reduction of NiFe_2O_4 to Ni and $\alpha\text{-Fe}$, the peak at 670 °C corresponds to the reduction of NiO species strongly interacting with $\gamma\text{-Al}_2\text{O}_3$ [48]. For the NiFe-IM catalysts, the peak at 355 °C is attributed to

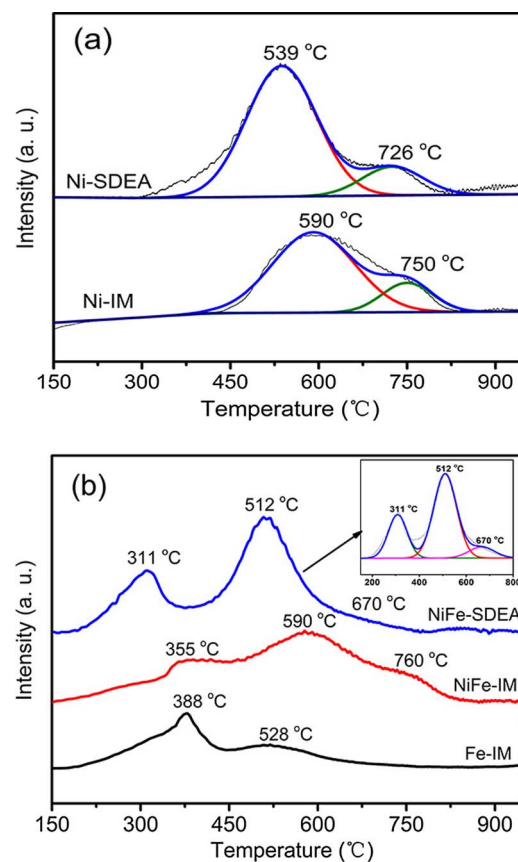


Fig. 4. H_2 -TPR spectra of Ni-SDEA and Ni-IM (a) and NiFe-SDEA, NiFe-IM and Fe-IM (b).

the reduction of $\alpha\text{-Fe}_2\text{O}_3$ to Fe_3O_4 ; the peak at 590 °C corresponds to the reduction of Fe_3O_4 , NiFe_2O_4 , and NiO species strongly interacting with $\gamma\text{-Al}_2\text{O}_3$ to $\alpha\text{-Fe}$, Ni and $\alpha\text{-Fe}$, and Ni, respectively; and the peak at 760 °C corresponds to the reduction of NiAl_2O_4 to Ni [48]. Compared with NiFe-IM, the hydrogen consumption peaks of NiFe-SDEA shift to much lower temperatures. The above results indicate that SDBS can effectively prevent a strong interaction between the metal oxides and $\gamma\text{-Al}_2\text{O}_3$ support. As a result, the generation of NiAl_2O_4 spinel phase through strong interaction with the support is inhibited, and more metal oxides are formed. Therefore, nickel species are more easily reduced and sulfided. Compared with the monometallic Ni-SDEA catalyst, the introduction of Fe promotes the reduction of Ni species in the bi-metallic NiFe-SDEA catalyst, because the interaction between NiO and Fe species can form NiFe_2O_4 , which is more easily reduced than NiO [20,49].

3.1.5. NH_3 -TPD

The NH_3 -TPD results indicate that Ni-SDEA and Ni-IM have almost the same acid strength (Fig. S5). The relative acid amounts of the two catalysts, which are listed in Table 1, are also almost the same.

3.1.6. Origin of highly dispersed NiO nanoparticles on Ni-SDEA

The Ni-SDEA catalyst prepared by the SDEA method has superior NiO dispersion, which is attributed to the de-agglomeration effect of SDBS (Fig. 5). The point of zero charge (PZC) of Al_2O_3 is pH = 8.4 [50,51], and hence, the Al_2O_3 surface has positive charges with a zeta potential of 18.3 mV at pH 5.0. Thus, electrostatic repulsion occurs between the positively charged Ni^{2+} ions and the electropositive Al_2O_3 surface, and it is therefore difficult for Ni^{2+} ions to adsorb onto the Al_2O_3 surface. After the introduction of SDBS, the negatively charged DBS⁻ ions could form self-assembled bilayers on the Al_2O_3 surface; one negative charge of these bilayers are connected with the electropositive

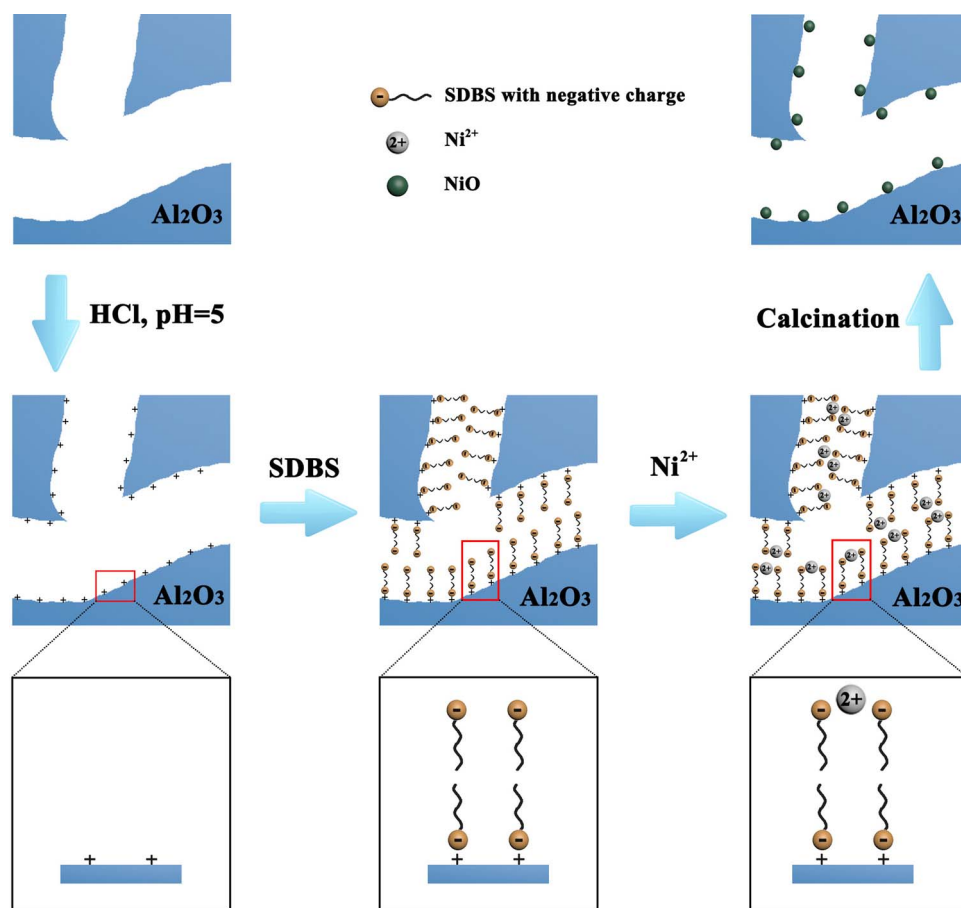


Fig. 5. Schematic diagram of the preparation principle of Ni-SDEA.

Al_2O_3 surface, and the other negative charge is exposed, as verified by the zeta potential of -13.7 mV on the surface of DBS⁻-modified alumina (Al_2O_3 -DBS) (Fig. 5). After the addition of Ni^{2+} ions, the electrostatic interaction between the Ni^{2+} ions and the electronegative Al_2O_3 -DBS surface induces the anchoring of Ni^{2+} ions on Al_2O_3 -DBS (Fig. 5). Furthermore, the long-chain alkyl groups in the bilayers can isolate the metals from the Al_2O_3 support, weakening the metal-support interaction and thus inhibiting the formation of nickel-aluminium spinels. During calcination in an air atmosphere, the slow combustion of surfactant produces a gaseous mixture that can be considered a protective barrier to inhibit the aggregation of metal species [52,53]. Meanwhile, a small amount of residual carbonaceous species is detected in the as-prepared Ni-SDEA catalyst (2.62 wt.%), the residual carbonaceous species plays an important role in isolating nickel species and preventing them from agglomeration [31].

In the conventional impregnation process, the acid solution is able to dissolve part of alumina, and thereby the surface hydrotalcite-type coprecipitation of Ni^{2+} ions with Al^{3+} is formed. The intimate contact between Ni and Al gives easily rise to NiAl_2O_4 under calcinations [54,55], as demonstrated by the above XPS characterization. As a result, the dispersion of supported NiO decreases, and Ni-IM thus possesses a low dispersion of large-sized NiO nanoparticles and a high content of nickel-aluminium spinels.

3.2. Characterization of the sulfided $\text{Ni}/\gamma\text{-Al}_2\text{O}_3$, $\text{NiFe}/\gamma\text{-Al}_2\text{O}_3$ and $\text{Fe}/\gamma\text{-Al}_2\text{O}_3$ catalysts

3.2.1. HRTEM

Representative HRTEM micrographs and the corresponding particle size distributions of supported metal nanoparticles over sulfided $\text{Ni}/\gamma\text{-Al}_2\text{O}_3$ and $\text{NiFe}/\gamma\text{-Al}_2\text{O}_3$ are shown in Figs. 6 and 7. White squares

denote some of the dark regions corresponding to Ni species (or NiS_x and NiFeS_x species) supported on the $\gamma\text{-Al}_2\text{O}_3$ surface (determined by EDS). In Fig. 6(a) and (b), the nanoparticles of the Ni species supported on NiS-SDEA are evenly dispersed with a concentrated size distribution between 2 and 4 nm, indicating the high dispersion of Ni nanoparticles over NiS-SDEA. However, the Ni nanoparticles supported on NiS-IM are aggregated into large clusters with a concentrated size distribution between 7 and 11 nm, as shown in Fig. 6(c) and (d), demonstrating the low dispersion of Ni nanoparticles over NiS-IM. According to Fig. 6(b) and (d), the mean sizes of the Ni nanoparticles over NiS-SDEA and NiS-IM are 2.8 and 7.9 nm, respectively. This result indicates that SDBS plays an important role in reducing the aggregation of Ni nanoparticles during the calcination and sulfidation steps.

In Fig. 7(a), the nanoparticles of NiFe species supported on NiFeS-SDEA are highly dispersed with an average particle size of 3.7 nm, demonstrating that the incorporation of Fe has little influence on the dispersion of the supported metal. NiFeS-IM possesses an average particle size of 11.5 nm, which is larger than that of NiFeS-SDEA. Additionally, the aggregation of the metal nanoparticles on NiFeS-IM is obvious, and the dispersion is poor. This result indicates that NiFeS-SDEA prepared by the SDEA method has considerably more NiS_x and NiFeS_x species than NiFeS-IM, which implies the superior thioetherification activity of NiFeS-SDEA. The HRTEM images of the used NiFeS-SDEA and NiFeS-IM catalysts demonstrate that the size and dispersion of metal nanoparticles over NiFeS-SDEA and NiFeS-IM are not changed after reaction for 144 h (Fig. S6).

3.2.2. XPS

Ni 2p XPS spectra of sulfided $\text{Ni}/\gamma\text{-Al}_2\text{O}_3$, $\text{NiFe}/\gamma\text{-Al}_2\text{O}_3$ and $\text{Fe}/\gamma\text{-Al}_2\text{O}_3$ are presented in Fig. 8. The binding energy at 853.2 eV is ascribed to the $2\text{p}_{3/2}$ level of NiS_x [56]. Compared with NiS-SDEA and

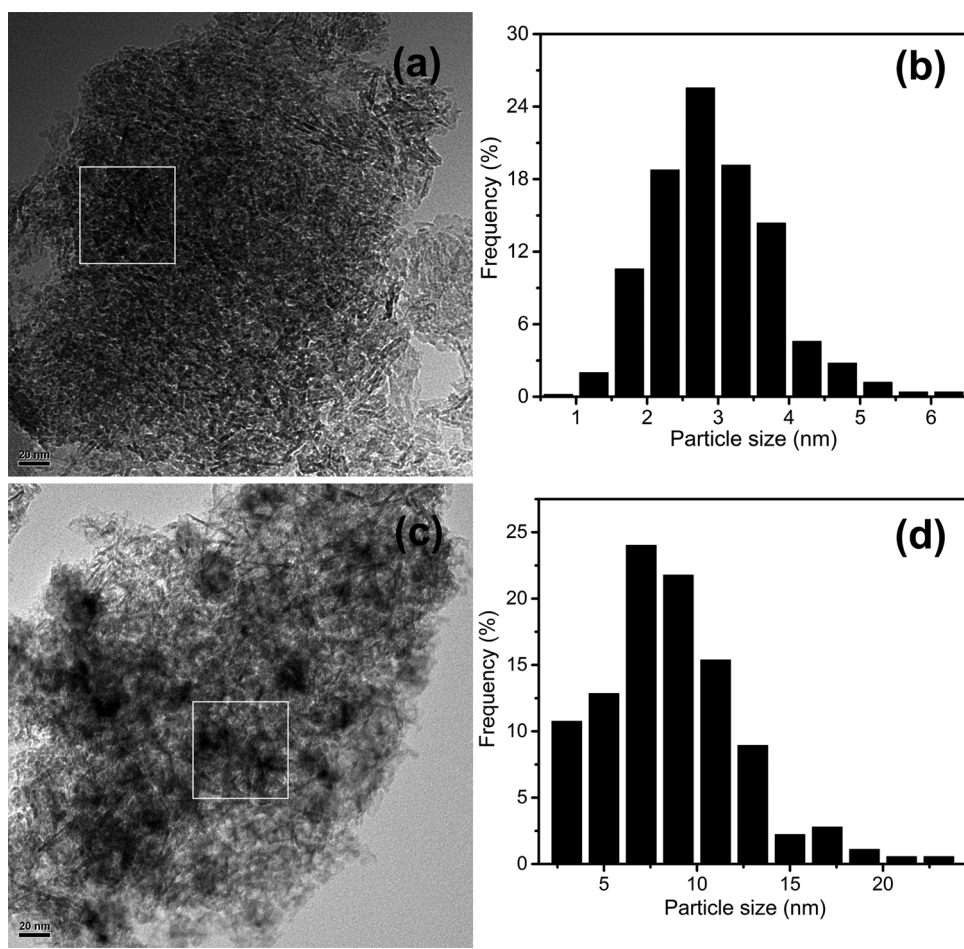


Fig. 6. HRTEM images and nanoparticle size distributions of NiS-SDEA (a and b) and NiS-IM (c and d).

NiS-IM, there is a new XPS peak at 853.8 eV attributed to Ni in NiFeS_x species in NiFeS-SDEA and NiFeS-IM [57]. The fitting results of the XPS spectra in Table 4 show that the content of NiS_x in NiS-IM is only 15.6% due to the strong interaction between Ni²⁺ and γ-Al₂O₃, which thus causes the low sulfidation degree of the nickel species. However, the content of NiS_x in NiS-SDEA is 34.6%, 2.22 times greater than that in NiS-IM, indicating that SDBS addition promotes the sulfidation of nickel species. The content of NiAl₂O₄ decreases from 57.8% in NiS-IM to 35.9% in NiS-SDEA, illustrating that the surfactant SDBS greatly inhibits the formation of inactive NiAl₂O₄ species. The contents of Ni in NiS_x and NiFeS_x increase from 16.6% and 11.0% for NiFeS-IM to 29.9% and 17.0% for NiFeS-SDEA, respectively (Table 5), demonstrating that the SDEA method promotes the formation of active sites for the thioetherification reaction.

Fig. 9 shows the experimental and fitted XPS spectra of S 2p for sulfided Ni/γ-Al₂O₃, NiFe/γ-Al₂O₃ and Fe/γ-Al₂O₃. The binding energies at 161.6, 162.3 and 163.5 eV are attributed to the 2p_{3/2} level of the monosulfide (S²⁻), disulfide (S₂²⁻), and polysulfide (S_n²⁻) species, respectively [58]. According to the calculated peak areas of fitted curves, the relative concentrations of different S species were derived, as presented in Tables 4 and 5. In NiS-SDEA and NiS-IM, the predominant S species are S²⁻ and S₂²⁻; the contents of S²⁻ and S₂²⁻ species in NiS-SDEA are 33.7 and 43.4%, whereas in NiS-IM the content of S²⁻ species increases to 53.2%, and the content of S₂²⁻ species decreases to 30.8%. The relative contents of S₂²⁻ in NiFeS-SDEA and NiFeS-IM are higher than those in NiS-SDEA, NiS-IM and FeS-IM. Compared with NiFeS-IM prepared by impregnation, NiFeS-SDEA has more S₂²⁻ species and less S²⁻ species bonded to metal atoms.

3.3. Catalytic activity of the sulfided Ni/γ-Al₂O₃, NiFe/γ-Al₂O₃ and Fe/γ-Al₂O₃ catalysts

The catalytic performances of the sulfided Ni/γ-Al₂O₃, NiFe/γ-Al₂O₃ and Fe/γ-Al₂O₃ catalysts for the thioetherification of 1-propanethiol and isoprene are shown in Table 6. NiS-SDEA has a mercaptan removal ratio of 90.2%, which is much higher than the 74.9% removal ratio obtained over NiS-IM. The mercaptan removal ratio of NiFeS-SDEA (99.5%) is higher than that of NiFeS-IM (85.1%). The mercaptan removal ratio of FeS-IM is as low as 43.6%, demonstrating the inferior thioetherification activity of this catalyst. The TOF value of NiS-SDEA is higher than that of NiS-IM (Table 6), indicating the better catalytic activity of NiS-SDEA. In view of the fact that the incorporation of Fe into the monometallic nickel catalysts improves the thioetherification activity, the TOF of the bimetallic catalysts are displayed in Table 6. The TOF of NiFeS-SDEA is higher than that of NiFeS-IM (Table 6), indicating the better catalytic activity of NiFeS-SDEA. NiS-SDEA, NiS-IM, NiFeS-SDEA, NiFeS-IM and FeS-IM have constant mercaptan removal ratio and olefin conversion, demonstrating their good activity stability (Figs. S7 and S8).

Furthermore, the olefin conversion over NiFeS-SDEA is 1.3%, which is slightly higher than those over NiS-SDEA, NiS-IM, NiFeS-IM and FeS-IM. The above results demonstrate that NiFeS-SDEA has an excellent mercaptan removal ratio and very low olefin conversion, indicating its outstanding selectivity for mercaptan removal.

The catalytic performances of the NiFeS-SDEA catalyst for the thioetherification of butanethiol isomers (1-butanethiol, iso-butanethiol and t-butanethiol) and isoprene are presented in Fig. 10. The mercaptan removal ratio over NiFeS-SDEA increases with the following sequence:

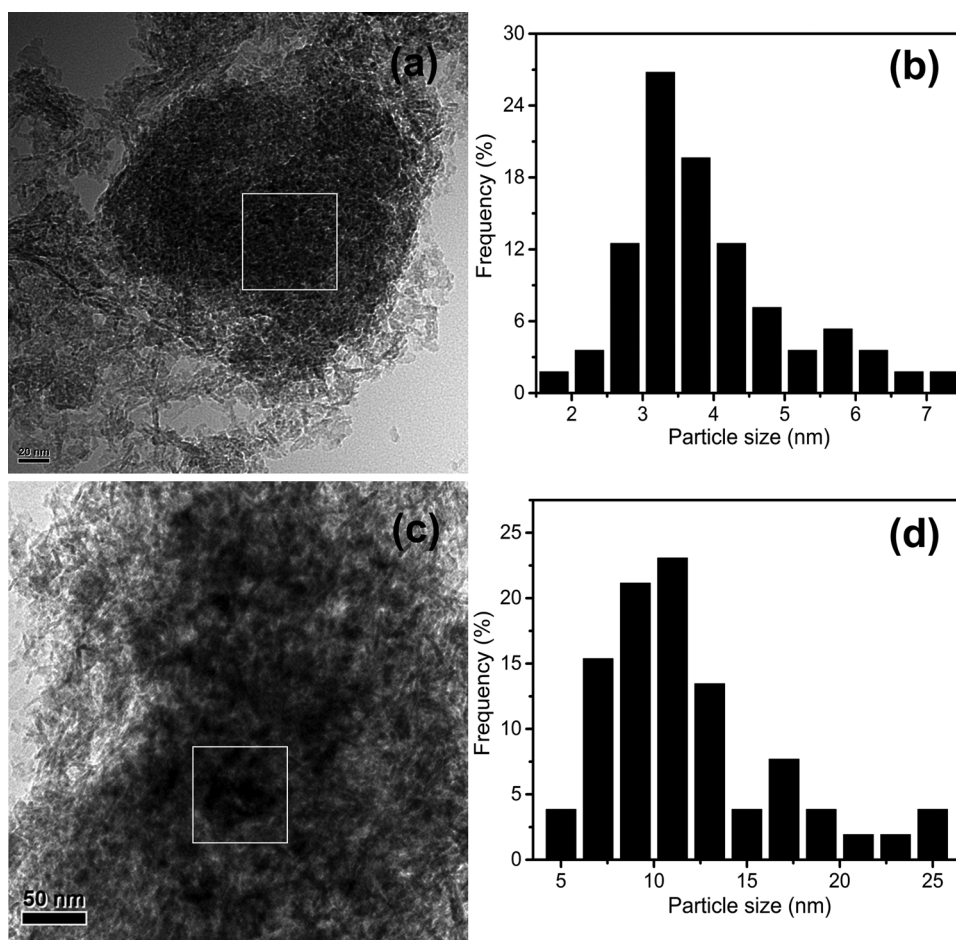


Fig. 7. HRTEM images and nanoparticle size distributions of NiFeS-SDEA (a and b) and NiFeS-IM (c and d).

t-butanethiol < iso-butanethiol < 1-butanethiol. Shen et al. reported the free-radical addition mechanism for thioetherification reaction [13], in which the steric hindrance of mercaptans is an important factor affecting the thioetherification activity. The steric hindrance of the mercaptans for the $-SH$ group increases with the following sequence: 1-butanethiol < iso-butanethiol < t-butanethiol [59], leading to more difficulty in C–S or S–H cleavage with greater steric hindrance around the $-SH$ group in mercaptan.

The thioetherification performances of the NiFeS-SDEA catalyst for the mercaptans with different alkyl chain lengths (1-propanethiol, 1-butanethiol and 1-pentanethiol) are presented in Fig. 11. The mercaptan removal ratio decreases with the increase in the number of carbon atoms in the alkyl chain. This is because with the increase of alkyl chain length, the steric hindrance around the $-SH$ group in mercaptan increases [60], and thereby the mercaptan with longer alkyl chain has worse reactivity.

3.4. Structure–activity correlation

The above thioetherification assessment results have demonstrated that catalyst NiS-SDEA has higher thioetherification activity than catalyst NiS-IM. To understand the different activities, it is necessary to correlate the thioetherification activities of the two catalysts with their structures. Since NiS-SDEA and NiS-IM have almost the same NiO loading, acid strength and acid amount (Fig. S5 and Table 1), the difference between the thioetherification activities of the two catalysts is related to the quantity and type of active sites. The enhanced activity of NiS-SDEA can be interpreted as follows: first, the dispersion of Ni on Ni-SDEA and Ni-IM are 17.9% and 8.2%, respectively. With a similar NiO

loading (13.8 wt.% for NiS-SDEA and 14.0 wt.% for NiS-IM, determined via ICP analysis), the higher dispersion of nickel on NiS-SDEA than on NiS-IM indicates that the former catalyst has smaller nickel particles than the latter catalyst, as demonstrated by the HRTEM images in Fig. 6. The number of active NiS_x sites on NiS-SDEA is greater than that on NiS-IM due to the smaller nanoparticles of Ni species and the higher dispersion of Ni nanoparticles on NiS-SDEA (Fig. 6). Second, among the S²⁻, S₂²⁻ and S_n²⁻ species, the binding energy of S²⁻ species is the lowest (Fig. 9), indicating that the S²⁻ species have the highest electron density and that accordingly, the Ni species bonded to S²⁻ species also have the highest electron density. Furthermore, the sulfur atom in mercaptan and the C=C double bond in olefins are electron rich [61]; therefore, the adsorption of the reactant molecules on the NiS species is weak, and thus, the activation of the reactant molecules is poor. As a consequence, the catalyst with more NiS species has an inferior activity for mercaptan removal. Among the three sulfur species, the binding energy of the S_n²⁻ species is the highest, demonstrating that the S_n²⁻ species have the lowest electron density and that accordingly, the Ni species bonded to S_n²⁻ species also have the lowest electron density. Therefore, the reactant molecules (mercaptan and diolefin) can be strongly adsorbed on the NiS_n species, and because of the electron-rich nature of the sulfur atom in thioethers, it is difficult for the generated thioether compounds to desorb from these active sites. As a consequence, the catalyst with more NiS_n species has an inadequate activity for mercaptan removal. Due to the electron migration of the Ni species with medium electron deficiency bonded to S₂²⁻, the electron density of S₂²⁻ species is optimal for the adsorption of reactant molecules and the desorption of products; consequently, the catalyst with more NiS₂ species should exhibit superior activity for mercaptan

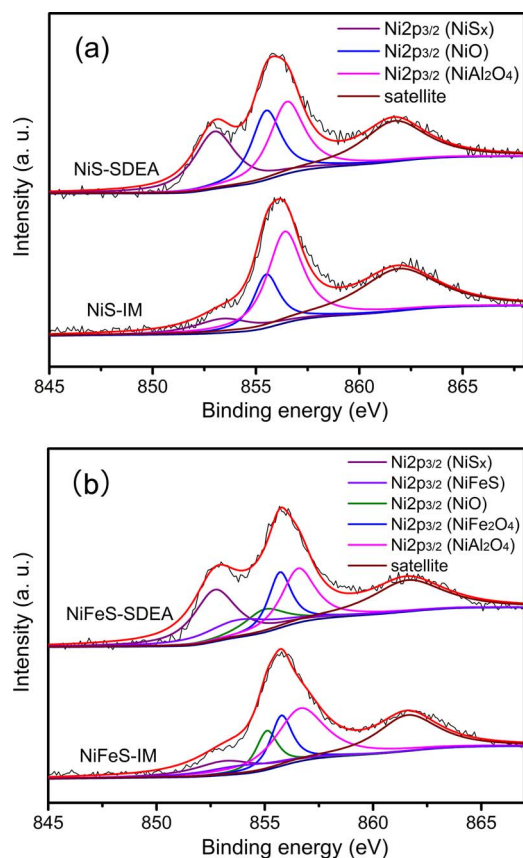


Fig. 8. Ni 2p XPS spectra of NiS-SDEA and NiS-IM (a) and NiFeS-SDEA and NiFeS-IM (b).

Table 4
XPS fitting results of NiS-SDEA and NiS-IM.

Catalyst	Ni 2p _{3/2} (%)			S 2p _{3/2} (%)		
	NiS _x	NiO	NiAl ₂ O ₄	S ²⁻	S ₂ ²⁻	S _n ²⁻
NiS-SDEA	34.6	29.5	35.9	33.7	43.4	22.9
NiS-IM	15.6	26.7	57.8	53.2	30.8	16.0

Table 5
XPS fitting results of NiFeS-SDEA, NiFeS-IM and FeS-IM.

Catalyst	Ni 2p _{3/2} (%)			S 2p _{3/2} (%)		
	NiS _x	NiFeS		S ²⁻	S ₂ ²⁻	S _n ²⁻
NiFeS-SDEA	29.9	17.0		24.1	58.4	17.5
NiFeS-IM	16.6	11.0		37.2	49.2	13.7
FeS-IM	–	–		13.0	23.2	63.8

removal. As seen in Table 4, the content of NiS₂ species over NiS-SDEA is higher than that over NiS-IM, supporting the higher mercaptan removal ratio over NiS-SDEA than over NiS-IM.

Because the introduction method and content of Fe in the two NiFe catalysts are the same, the greater catalytic activity of catalyst NiFeS-SDEA is attributed to the SDEA method used for loading Ni species. On the one hand, the introduction of SDBS is advantageous for the formation and dispersion of uniform Ni and NiFe species (demonstrated by the HRTEM images in Fig. 7), and the resulting smaller and more highly dispersed Ni and NiFe nanoparticles over NiFeS-SDEA than over NiFeS-IM (Fig. 7) provide a higher content of active sites. On the other hand, the SDEA method can inhibit the formation of inactive NiAl₂O₄ species (Fig. 4(b)), which increases the content of active NiS_x and NiFeS_x sites.

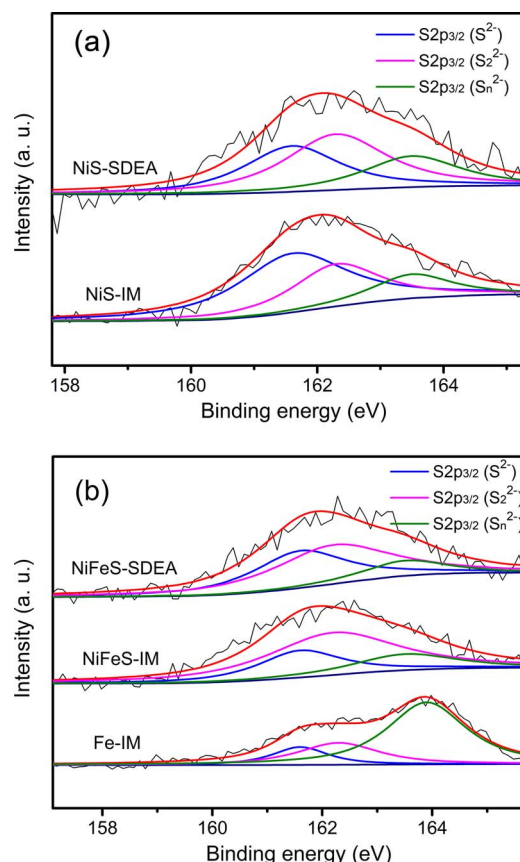


Fig. 9. S 2p XPS spectra of NiS-SDEA and NiS-IM (a) and NiFeS-SDEA, NiFeS-IM and FeS-IM (b).

Table 6
Thioetherification reaction results over the Ni, NiFe and Fe catalysts.

Catalyst	mercaptop removal ratio (%)	olefin conversion (%)	TOF (10^{-3} s ⁻¹)
NiS-SDEA	90.2	1.1	2.65
NiS-IM	74.9	0.7	1.82
NiFeS-SDEA	99.5	1.3	3.32
NiFeS-IM	85.1	0.9	2.76
FeS-IM	43.6	0.5	–

As shown in Table 5, the content of S₂²⁻ species over NiFeS-SDEA is 58.4%, which is higher than 49.2% over NiFeS-IM. Over NiFeS-SDEA, the Fe atoms interact with the highly dispersed NiS_x species that possess a higher content of active NiS₂ sites (Table 5), and thereby the active NiFeS_x sites over NiFeS-SDEA are mainly composed of NiFeS₂ species (Table 5). Among the NiS_x and NiFeS_x active sites, the NiS and NiFeS active sites have an inferior activity for mercaptan removal, because the Ni and NiFe bonded to S²⁻ species have the highest electron density (Fig. 9) and resultant poor activation ability for mercaptan; the NiS_n and NiFeS_n active sites have a low activity for mercaptan removal due to the lowest electron density of the Ni and NiFe bonded to S_n²⁻ species (Fig. 9), resulting in the difficult desorption of the generated thioether compounds from these active sites; the NiS₂ and NiFeS₂ active sites exhibit superior activity for mercaptan removal because of the optimal activation of reactant molecules and the easy desorption of product molecules. It is the higher content of NiS₂ and NiFeS₂ species over NiFeS-SDEA than over NiFeS-IM (Table 5) that leads to the better mercaptan removal over NiFeS-SDEA than over NiFeS-IM. The above two effects greatly improve the thioetherification activity of NiFeS-SDEA.

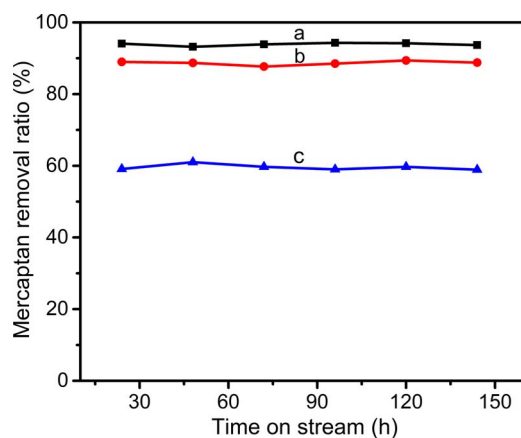


Fig. 10. Thioetherification performances of NiFeS-SDEA for 1-butanethiol (a), iso-butanethiol (b) and t-butanethiol (c).

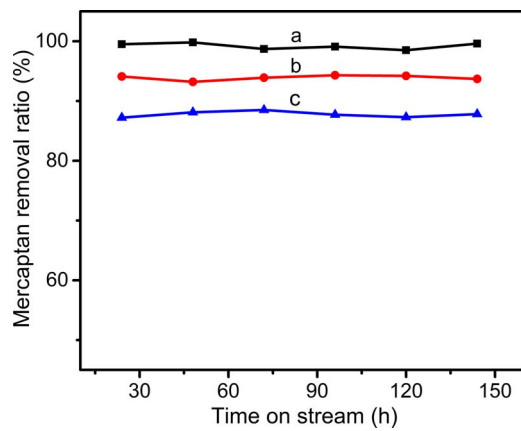


Fig. 11. Thioetherification performances of NiFeS-SDEA for 1-propanethiol (a), 1-butanethiol (b) and 1-pentanethiol (c).

The product distributions of NiS-SDEA and NiS-IM are listed in Table 7. The sulfur types in the product obtained over the two catalysts are similar: the main type of sulfur-containing compound is C_3SC_5 (pathway I, IV and VI), and the product also contains some thioether C_3SC_3 (pathway III) and C_5SC_5 (pathway V), as well as dimethyl sulfide species C_3SSC_3 (pathway II). According to the above results, the reaction pathways for the thioetherification of 1-propanethiol can be inferred as follows (Fig. 12): S–H bond scission of 1-propanethiol generates dissociated C_3S^* and $*H$ groups [62,63]; subsequently, the C_3S^* species interacts with C_5^* that originate from the activation of adsorbed isoprene, and thus, C_3SC_5 species are generated (pathway I). Meanwhile, some dimethyl sulfide species, C_3SSC_3 , are formed via the coupling of two C_3S^* species on active NiS_x sites (pathway II). In addition, the breaking of the C–S bond in 1-propanethiol also occurs, generating dissociated C_3^* and $*SH$; the former species interacts with dissociated C_5S^* and generates C_3SC_3 (pathway III). Todorova et al. proposed that the generated $*SH$ could interact with the adsorbed olefin intermediate

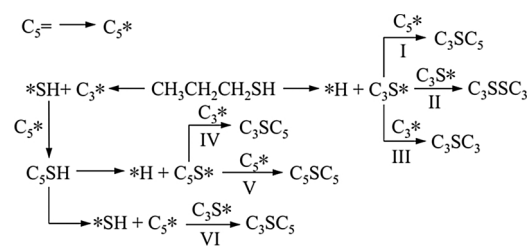


Fig. 12. Thioetherification reaction network of 1-propanethiol.

through a reverse reaction and produce new mercaptans [64]; thus, $*SH$ could interact with C_5^* and form pentanethiol C_5SH , and then C_5SH could participate in the above reactions (S–H bond scission and C–S bond scission) immediately. The S–H bond scission generates dissociated C_3S^* and $*H$ groups, and C_3S^* interacts with C_5^* and C_5^* to form C_3SC_5 (pathway IV) and C_5SC_5 (pathway V), respectively; C–S bond scission generates C_5^* and $*SH$ species, and C_5^* interacts with C_3S^* to form C_3SC_5 (pathway VI).

The contents of C_3SSC_3 , C_3SC_3 and C_5SC_5 over NiS-IM are higher than those over NiS-SDEA, indicating that NiS-IM has higher content of C_3S^* and C_5S^* species in reaction than NiS-SDEA. Thus, NiS-IM exhibits better ability to cleave the S–H bond of mercaptan than NiS-SDEA. C_3SC_5 can be formed by the pathways I, IV and VI, and the pathways I and IV are the S–H bond scission reaction [13]. Because NiS-SDEA has inferior ability to cleave the S–H bond of mercaptan compared with NiS-IM, the higher content of C_3SC_5 over NiS-SDEA than that over NiS-IM should be attributed to the enhanced pathway VI that is the C–S bond scission reaction [13]. Thus, NiS-SDEA has better ability to cleave the C–S bond of mercaptan than NiS-IM. According to the XPS characterization results, the content of S_2^{2-} species in NiS-SDEA is higher than that in NiS-IM, whereas the content of S^{2-} species in NiS-SDEA is lower than that in NiS-IM. The above reaction results suggest that a high content of S_2^{2-} species enhances the C–S bond scission of mercaptan, while a high content of S^{2-} species improves the S–H bond scission of mercaptan.

4. Conclusions

A novel SDBS-assisted equilibrium adsorption method is proposed to prepare monometallic Ni/Al_2O_3 and Fe-promoted $NiFe/Al_2O_3$ catalysts with high metal dispersion and a weak metal-alumina interaction. In this method, nickel cations are anchored onto the electronegative DBS⁻-modified Al_2O_3 support (Al_2O_3 -DBS), and the aggregation of Ni nanoparticles during calcination is prevented by the isolation effect of carbonaceous species. Furthermore, this method weakens the metal-support interaction and reduces the formation of nickel-aluminium spinels because it decreases the direct interaction between Ni species and the alumina support. As a consequence, the active Ni and NiFe sites are highly dispersed on the surface of Al_2O_3 -DBS with an enhanced reducibility and sulfurization degree. The corresponding Ni-based catalysts prepared by this method exhibit much higher activity and selectivity for mercaptan removal than their counterparts prepared by the conventional impregnation method.

Acknowledgment

The authors gratefully acknowledge the financial support of the National Natural Science Foundation of China (Grant Nos. 21076228 and U1162116).

Appendix A. Supplementary data

Supplementary material related to this article can be found, in the online version, at doi:<https://doi.org/10.1016/j.apcatb.2018.02.053>.

Table 7
Product distributions of NiS-SDEA and NiS-IM catalysts.

Catalyst	Product selectivity ^a (%)			
	C_3SC_3	C_3SC_5	C_3SSC_3	C_5SC_5
NiS-SDEA	3.74	85.78	3.55	6.93
NiS-IM	6.19	75.64	7.19	10.98

^a Determined at about 50% of the 1-propanethiol conversion by changing liquid hourly space velocity.

References

- [1] J. Xu, T. Huang, Y. Fan, *Appl. Catal. B Environ.* 203 (2017) 839–850.
- [2] R. Singh, D. Kunzru, S. Sivakumar, *Appl. Catal. B Environ.* 185 (2016) 163–173.
- [3] T. Huang, J. Xu, Y. Fan, *Appl. Catal. B Environ.* 220 (2018) 42–56.
- [4] J.N. Díaz de León, L.A. Zavala-Sánchez, V.A. Suárez-Torillo, G. Alonso-Núñez, T.A. Zepeda, R.I. Yocupicio, J.A. de los Reyes, S. Fuentes, *Appl. Catal. B Environ.* 213 (2017) 167–176.
- [5] Y. Zhang, Z. Liu, W. Wang, Z. Cheng, B. Shen, *Fuel Process. Technol.* 115 (2013) 63–70.
- [6] L. Gao, Q. Xue, Y. Liu, Y. Lu, *AIChE J.* 55 (2009) 3214–3220.
- [7] S. Wang, Y. Fan, X. Jia, *Chem. Eng. J.* 256 (2014) 14–22.
- [8] A. Leitão, A. Rodrigues, *Chem. Eng. Sci.* 44 (1989) 1245–1253.
- [9] J.C. Bricker, L. Laricchia, *Top. Catal.* 55 (2012) 1315–1323.
- [10] S. Magyar, J. Hancsók, D. Kalló, *Fuel Process. Technol.* 86 (2005) 1151–1164.
- [11] M. Toba, Y. Miki, Y. Kanda, T. Matsui, Y. Yoshimura, *Catal. Today* 104 (2005) 64–69.
- [12] S. Brunet, D. Mey, G. Pérrot, C. Bouchy, F. Diehl, *Appl. Catal. A Gen.* 278 (2005) 143–172.
- [13] Z. Shen, M. Ke, P. Yu, H. Hu, Q. Jiang, *J. Mol. Catal. A Chem.* 396 (2015) 120–127.
- [14] T. Imai, J.C. Bricker, US Patents (1988) 4775462.
- [15] S. Frey, US Patents (1998) 5759386.
- [16] H.S. Cerqueira, G. Caeiro, L. Costa, F.R. Ribeiro, *J. Mol. Catal. A Chem.* 292 (2008) 1–13.
- [17] R.L. Wilson, C. Kemball, *J. Catal.* 3 (1964) 426–437.
- [18] P. Kieran, C. Kemball, *J. Catal.* 4 (1965) 380–393.
- [19] C.M. Fu, A.M. Schaffer, *Ind. Eng. Chem. Prod. Res. Dev.* 24 (1985) 68–75.
- [20] D. Huang, M. Ke, X. Bao, H. Liu, *Ind. Eng. Chem. Res.* 55 (2016) 1192–1201.
- [21] A.J. Akande, R.O. Idem, A.K. Dalai, *Appl. Catal. A Gen.* 287 (2005) 159–175.
- [22] P.G. Savva, K. Goundani, J. Vakros, K. Bourikas, Ch. Fountzoula, D. Vattis, A. Lycurghiotis, Ch. Kordulis, *Appl. Catal. B Environ.* 79 (2008) 199–207.
- [23] R. Loe, E. Santillan-Jimenez, T. Morgan, L. Sewell, Y. Ji, S. Jones, M.A. Isaacs, A.F. Lee, M. Crocker, *Appl. Catal. B Environ.* 191 (2016) 147–156.
- [24] J.G. Seo, M.H. Youn, H.I. Lee, J.J. Kim, E. Yang, J.S. Chung, *Chem. Eng. J.* 141 (2008) 298–304.
- [25] G. Wu, C. Zhang, S. Li, Z. Han, T. Wang, X. Ma, J. Gong, *ACS Sustain. Chem. Eng.* 1 (2013) 1052–1062.
- [26] G. Li, L. Hu, J.M. Hill, *Appl. Catal. A Gen.* 301 (2006) 16–24.
- [27] X. Zhu, P. Huo, Y. Zhang, D. Cheng, C. Liu, *Appl. Catal. B Environ.* 81 (2008) 132–140.
- [28] J.G. Seo, M.H. Youn, J.C. Jung, I.K. Song, *Int. J. Hydrogen Energy* 35 (2010) 6738–6746.
- [29] F. Frusteri, M. Cordaro, C. Cannilla, G. Bonura, *Appl. Catal. B Environ.* 162 (2015) 57–65.
- [30] J. Lif, M. Skoglundh, L. Löwendahl, *Appl. Catal. A Gen.* 228 (2002) 145–154.
- [31] H. Li, M. Li, Y. Chu, F. Liu, H. Nie, *Appl. Catal. A Gen.* 403 (2011) 75–82.
- [32] J.E. Casillas, F. Tzompantzi, S.G. Castellanos, G. Mendoza-Damián, R. Pérez-Hernández, A. López-Gaona, A. Barrera, *Appl. Catal. B Environ.* 208 (2017) 161–170.
- [33] Y. Fan, H. Xiao, G. Shi, H. Liu, X. Bao, *Energy Environ. Sci.* 4 (2011) 572–582.
- [34] X. Wang, X. Li, X. Sun, F. Li, Q. Liu, Q. Wang, D. He, *J. Mater. Chem.* 21 (2011) 3571–3573.
- [35] I.C. Freitas, R.L. Manfro, M.M.V.M. Souza, *Appl. Catal. B Environ.* 220 (2018) 31–41.
- [36] J. Wang, G. Yang, L. Wang, W. Yan, *J. Mater. Chem. A* 4 (2016) 8620–8629.
- [37] F. Liu, S. Xu, L. Cao, Y. Chi, T. Zhang, D. Xue, *J. Phys. Chem. C* 111 (2007) 7396–7402.
- [38] R. Hernández-Huesca, J. Mérida-Robles, P. Maireles-Torres, E. Rodríguez-Castellón, A. Jiménez-López, *J. Catal.* 203 (2001) 122–132.
- [39] J. Ashok, S. Kawi, *ACS Catal.* 4 (2014) 289–301.
- [40] N.S. McIntyre, M.G. Cook, *Anal. Chem.* 47 (1975) 2208–2213.
- [41] H. Lee, J.C. Jung, H. Kim, Y.M. Chung, T.J. Kim, S.J. Lee, S.H. Oh, Y.S. Kim, I.K. Song, *Catal. Lett.* 124 (2008) 364–368.
- [42] A.S. Reddy, C.Y. Chen, C.C. Chen, S.H. Chien, C.J. Lin, K.H. Lin, C.L. Chen, S.C. Chang, *J. Mol. Catal. A Chem.* 318 (2010) 60–67.
- [43] T. Tong, J. Zhang, B. Tian, F. Chen, D. He, *J. Hazard. Mater.* 155 (2008) 572–579.
- [44] P.J. Mangnus, A. Bos, J.A. Moulijn, *J. Catal.* 146 (1994) 437–448.
- [45] B. Scheffer, P. Molhoek, J.A. Moulijn, *Appl. Catal.* 46 (1989) 11–30.
- [46] T.V. Voskoboinikov, H.Y. Chen, W.M.H. Sachtler, *Appl. Catal. B Environ.* 19 (1998) 279–287.
- [47] F. Liu, H. He, C. Zhang, Z. Feng, L. Zheng, Y. Xie, T. Hu, *Appl. Catal. B Environ.* 96 (2010) 408–420.
- [48] T. Li, H. Wang, Y. Yang, H. Xiang, Y. Li, *Fuel Process. Technol.* 118 (2014) 117–124.
- [49] S. Hwang, U.G. Hong, J. Lee, J.H. Baik, D.J. Koh, H. Lim, I.K. Song, *Catal. Lett.* 142 (2012) 860–868.
- [50] M. Kosmulski, J. Colloid, *Interface Sci.* 253 (2002) 77–87.
- [51] J. Vakros, K. Bourikas, Ch. Kordulis, A. Lycurghiotis, *J. Phys. Chem. B* 107 (2003) 1804–1813.
- [52] Y. Zhai, S. Zhang, H. Pang, *Mater. Lett.* 61 (2007) 1863–1866.
- [53] J. Xu, Y. Guo, T. Huang, Y. Fan, *Chem. Eng. J.* 333 (2018) 206–215.
- [54] J.W. Geus, G. Poncellet, P.A. Jacobs, P. Grange (Eds.), *Preparation of Catalysts III*, Elsevier, Amsterdam, 1983, p. 6.
- [55] P.K. De Bokx, W.B.A. Wassenberg, J.W. Geus, *J. Catal.* 104 (1987) 86–98.
- [56] M. Sun, T. Bürgi, R. Cattaneo, D. van Langeveld, R. Prins, *J. Catal.* 201 (2001) 258–269.
- [57] H.R. Reinhoudt, E. Crezee, A.D. van Langeveld, P.J. Kooyman, J.A.R. van Veen, J.A. Moulijn, *J. Catal.* 196 (2000) 315–329.
- [58] F. Liao, J. Świątowska, V. Maurice, A. Seyeux, L.H. Klein, S. Zanna, P. Marcus, *Appl. Surf. Sci.* 283 (2013) 888–899.
- [59] C.C. Wamser, R.T. Medary, I.E. Kochevar, N.J. Turro, P.L. Chang, *J. Am. Chem. Soc.* 97 (1975) 4864–4869.
- [60] M.U. Islam, S. Khan, M.W. Ullah, J.K. Park, *J. Chem. Soc. Pak.* 37 (2015) 1040–1046.
- [61] E. Krebs, B. Silvi, A. Daudin, P. Raybaud, *J. Catal.* 260 (2008) 276–287.
- [62] P. Kieran, C. Kemball, *J. Catal.* 4 (1965) 380–393.
- [63] T.S. Rafael, D.R. Huntley, D.R. Mullins, J.L. Gland, *J. Phys. Chem.* 99 (1995) 11472–11480.
- [64] T. Todorova, R. Prins, T. Weber, *J. Catal.* 246 (2007) 109–117.